

## Article

# Electrochemical Biosensor for Markers of Neurological Esterase Inhibition

Neda Rafat <sup>1,2</sup>, Paul Satoh <sup>1</sup> and Robert Mark Worden <sup>1,2,3,\*</sup>

<sup>1</sup> Department of Chemical Engineering and Materials Science, Michigan State University, 428 S. Shaw Lane, East Lansing, MI 48824, USA; rafatned@msu.edu (N.R.); satoh@msu.edu (P.S.)

<sup>2</sup> The Institute for Quantitative Health Science and Engineering, Michigan State University, 775 Woodlot Dr, East Lansing, MI 48824, USA

<sup>3</sup> Department of Biomedical Engineering, Michigan State University, 775 Woodlot Dr, East Lansing, MI 48824, USA

\* Correspondence: worden@msu.edu; Tel.: +1-(517)-242-8117

**Abstract:** A novel, integrated experimental and modeling framework was applied to an inhibition-based bi-enzyme (IBE) electrochemical biosensor to detect acetylcholinesterase (AChE) inhibitors that may trigger neurological diseases. The biosensor was fabricated by co-immobilizing AChE and tyrosinase (Tyr) on the gold working electrode of a screen-printed electrode (SPE) array. The reaction chemistry included a redox-recycle amplification mechanism to improve the biosensor's current output and sensitivity. A mechanistic mathematical model of the biosensor was used to simulate key diffusion and reaction steps, including diffusion of AChE's reactant (phenylacetate) and inhibitor, the reaction kinetics of the two enzymes, and electrochemical reaction kinetics at the SPE's working electrode. The model was validated by showing that it could reproduce a steady-state biosensor current as a function of the inhibitor (PMSF) concentration and unsteady-state dynamics of the biosensor current following the addition of a reactant (phenylacetate) and inhibitor phenylmethylsulfonylfluoride). The model's utility for characterizing and optimizing biosensor performance was then demonstrated. It was used to calculate the sensitivity of the biosensor's current output and the redox-recycle amplification factor as a function of experimental variables. It was used to calculate dimensionless Damkohler numbers and current-control coefficients that indicated the degree to which individual diffusion and reaction steps limited the biosensor's output current. Finally, the model's utility in designing IBE biosensors and operating conditions that achieve specific performance criteria was discussed.

**Keywords:** amperometric biosensor; neural esterase; acetylcholinesterase; inhibition; organophosphate; design; optimization; mathematical model; flux control; dimensionless



**Citation:** Rafat, N.; Satoh, P.; Worden, R.M. Electrochemical Biosensor for Markers of Neurological Esterase Inhibition. *Biosensors* **2021**, *11*, 459. <https://doi.org/10.3390/bios11110459>

Received: 30 August 2021

Accepted: 8 November 2021

Published: 16 November 2021

**Publisher's Note:** MDPI stays neutral with regard to jurisdictional claims in published maps and institutional affiliations.



**Copyright:** © 2021 by the authors. Licensee MDPI, Basel, Switzerland. This article is an open access article distributed under the terms and conditions of the Creative Commons Attribution (CC BY) license (<https://creativecommons.org/licenses/by/4.0/>).

## 1. Introduction

Electrochemical biosensors are analytical devices that detect analytes by transforming a biochemical reaction into a quantitative, electrical signal. They integrate the specificity of biological recognition molecules (e.g., antibodies) with the advantages of electrochemical detection techniques [1,2]. Electrochemical biosensors benefit from several advantages, such as low cost, ease of use, portability, and simplicity of construction. These advantages make electrochemical biosensors great options for the development of analytical devices in different fields [3,4]. Some of the limitations for electrochemical biosensors are limited shelf life, narrow or limited temperature range for operation, and sometimes high sensitivity of detection results in false-positive results [5]. The electrochemical biosensors can be divided into four major categories based on the electrochemical technique that is used to measure the electrical signal produced by the biochemical mechanism: amperometric biosensors, potentiometric biosensors, conductometric biosensors, and impedimetric biosensors [6].

Amperometric biosensors detect chemicals at a constant electrochemical potential by measuring the oxidation or reduction current produced by electroactive products of a biochemical reaction [7]. Their low cost, high sensitivity, fast response time, simplicity of design, compactness, and potential for miniaturization make amperometric biosensors well suited for detecting a wide range of chemicals and biochemical agents, including disease markers [8,9].

Amperometric biosensors that measure analytes indirectly by their inhibition of target enzymes have been developed for environmental and healthcare applications [10]. Such inhibition-based biosensors can be very sensitive when the target enzyme is inhibited by a very low concentration of its inhibitor [11]. For that reason, significant research has been devoted to developing amperometric biosensors that measure markers of neurological disease processes that inhibit neural esterases, such as acetylcholinesterase (AChE) [12–17].

Some organophosphate compounds (OPs) are potent inhibitors of neural esterases and, for that reason, are used as pesticides and as chemical weapons [18]. The well-known neural esterase acetylcholinesterase (AChE) breaks down the neurotransmitter acetylcholine, which chemically relays an impulse across the synapse between two neurons [19]. The inhibition of AChE by OPs prevents acetylcholine hydrolysis, resulting in continuous nerve firing, which can cause severe, acute health issues, including death [20]. Each year, approximately 3 million people are poisoned by organophosphates, accounting for 300,000 deaths worldwide [21].

The gold standard analytical method for OPs is gas/liquid chromatography combined with mass spectroscopy [22]. This method is sensitive, specific, and reliable. However, it is not well suited for many on-site applications because it requires bulky, expensive equipment and involves complicated and time-consuming sample processing by trained technicians [22]. In contrast, inhibition-based amperometric biosensors offer the potential to measure OPs on-site rapidly, inexpensively, with minimal sample processing using a miniature electronic device similar to a personal blood-glucose meter [23].

When an enzyme is strongly inhibited by a specific substance, it may be possible to develop an inhibition-based enzyme biosensor that can specifically detect the presence of the inhibitor in a complex mixture that may include unknown chemicals or pollutants. However, for enzymes that are sensitive to multiple inhibitors, this approach cannot discern which inhibitor(s) is present in the mixture.

Although amperometric biosensors might not offer the same sensitivity and specificity of detection that gas/liquid chromatography-based techniques offer, the fact that they can be developed as portable diagnostic devices for quick and cost-effective initial analysis makes them valuable for initial screening and monitoring. Commercialized miniaturized potentiostats and screen-printed electrodes (SPEs) can be used to develop portable amperometric biosensor systems. SPEs include one or more printed working electrodes, a reference electrode, and a counter electrode printed on a solid substrate. The assay chemistry is performed on the working electrode, and the electrochemical assay is conducted by contacting the SPE with a sample solution. SPEs can replace bulky convention electrochemical cells with a miniaturized system that can be used for simple and quick electrochemical measurements. However, because SPEs are designed to minimize the required space and reagent volume, their measurements are often not as stable and accurate as those conducted in a conventional electrochemical cell.

Research to rationally design and optimize amperometric biosensors for detecting inhibitors of AChE or other neural esterases (e.g., butyryl esterase) has been hampered by the lack of a comprehensive mathematical model able to predict the rates of potentially rate-limiting mass-transfer and chemical reaction steps that produce the amperometric signal. Zhang et al. developed a theoretical model for immobilized-enzyme-inhibition biosensors under the assumption that the inhibition process is diffusion-limited [24]. Choi et al. developed a mathematical model for a fiber-optic biosensor to detect OPs. This model, which simulated both AChE inhibition kinetics and diffusion, was able to optimize the concentrations of AChE and its substrate [25].

We recently developed a novel, integrated experimental and modeling framework that includes a steady-state, mechanistic mathematical model that describes the rate of key mass-transfer and reaction steps and a novel dimensional-analysis approach to assess the degree to which individual mass-transfer and reaction steps limit the biosensor's amplitude and sensitivity [26]. We then demonstrated the framework's utility using a novel amperometric electrochemical immunosensor.

In this paper, we apply the framework to an inhibition-based bi-enzyme (IBE) amperometric biosensor assembled on a s SPE. The IBE interface contained a neural esterase (AChE) and an oxidase enzyme (tyrosinase) that generates a redox-reaction loop to amplify the biosensor's output [27–29]. We present a novel, unsteady-state model of the IBE biosensor that consists of unsteady-state mass balance equations describing the mass-transfer and reaction steps that govern the biosensor's signal. We use experimental results to validate the model and discuss the utility of dimensionless groups based on the model, including current-control coefficients, sensitivity coefficients, and Damkohler numbers, to rationally design and optimize IBE biosensors.

## 2. Materials and Methods

### 2.1. Materials

Sodium phosphate (monobasic and dibasic), AChE (C2888, from *Electrophorus electricus*), tyrosinase (T3824, from mushroom), bovine serum albumin (BSA), glutaric dialdehyde (50 wt.% solution in water), PMSF, and phenylacetate were obtained from Sigma Aldrich (St. Louis, MO, USA). Ultrapure water (18.2 M $\Omega$ ) was produced by a Nanopure-UV four-stage purifier (Barnstead International, Dubuque, IA, USA); the purifier was equipped with a UV source and a final 0.2  $\mu$ m filter. Ultrapure water was used to prepare all aqueous solutions. Screen-printed electrodes were obtained from Conductive Technologies Inc. (New York, NY, USA). and Metrohm DropSens (models DRP-250AT, Asturias, Spain).

### 2.2. Enzyme Electrode Preparation

SPEs were selected as the platform for conducting the experiments for two reasons. First, SPEs are small, inexpensive, and disposable, making them well-suited for POC applications. Second, SPEs are often used in the development of commercialized electrochemical biosensors. SPEs were cleaned by sonication in pure ethanol for 2 min followed by rinsing with ultrapure water. Different types of SPEs, including carbon (DPR-C110), low temperature cured gold (DRP-220BT), high temperature cured gold SPEs (DRP-250AT), and carbon nanotube-modified (DRP-10SWCNT), were tried for the fabrication of the biosensor. The immobilization technique used in this work was based on the crosslinking of two enzymes with glutaraldehyde and bovine serum albumin (BSA) [30]. This technique resulted in an efficient and rapid comobilization of two enzymes. Although this technique worked on all types of SPEs, DPR-250AT resulted in a better repeatability of data. To optimize the immobilization method, a variety of BSA concentrations, glutaraldehyde concentrations, and ratios of AChE to tyrosinase were studied.

To prepare the enzyme solution, 40  $\mu$ L of 50 mM phosphate buffer pH 7, 20  $\mu$ L of 20 mg/mL tyrosinase in phosphate buffer, 20  $\mu$ L of 1 mg/mL AChE in phosphate buffer, 10  $\mu$ L of 2.7 mg/mL BSA in phosphate buffer, and 10  $\mu$ L of 4 wt.% glutaraldehyde in water were mixed together just before starting the preparation procedure. To obtain the optimized concentration of the two enzymes, BSA, and glutaraldehyde, 3  $\mu$ L of enzyme solution (in the case of DropSens SPEs) or 1  $\mu$ L of enzyme solution (in the case of CTI SPEs) were deposited on the working electrode, and the SPEs were left at 4  $^{\circ}$ C to dry overnight. The next day, the prepared bi-enzyme-modified SPEs were rinsed with ultrapure water and then stored in phosphate buffer at 4  $^{\circ}$ C.

### 2.3. PMSF Detection and Electrochemical Measurements

PMSF is used as a model AChE inhibitor because it is less toxic to humans than many OPs. Its reaction mechanism is similar to that of OPs, but its sulfonamide bond with serine's hydroxyl group in the AChE active site is more stable than a typical OP linkage.

To conduct the electrochemical measurements, the desired electrochemical potential was applied on the SPE's working electrode relative to the SPE's printed pseudo-Ag/AgCl reference electrode. The SPE's counter electrode served as the anode, so the biosensor's current would not flow through the reference electrode and change its potential. In experiments to detect AChE inhibition by PMSF, 30  $\mu\text{L}$  of 50 mM phosphate buffer (pH 7) was added to the IBE SPE biosensors. A potential of  $-200$  mV relative to an Ag/AgCl reference electrode was maintained on the working electrode using a potentiometer (CHI 660, C.H. Instruments, Austin, TX, USA). An aliquot of phenylacetate solution was added to initiate the IBE's amperometric signal. Then, after a stable electrochemical signal was obtained, a known amount of PMSF was added while continuously recording the electrochemical current as a function of time. The experiments were repeated in triplicate, and steady-state current values were reported as the mean  $\pm$  standard deviation of three replicates.

### 2.4. Mechanistic Mathematical Model of the IBE Biosensor Interface

The biosensor's conceptual model (Figure 1) includes a working electrode onto which an enzyme-containing layer of thickness  $L$  is bound, a diffusion layer having thickness  $\delta$ , and the bulk solution. AChE ( $E_1$ ) hydrolyzes the reactant phenylacetate ( $S_1$ ) to give phenol ( $S_2$ ) (Figure 2), which is then oxidized twice by tyrosinase ( $E_2$ )—first to catechol ( $S_4$ ) and then to o-quinone ( $S_3$ ). The  $S_4$  can then be reduced back to  $S_3$  at the electrode, generating the biosensor's output current. This current is amplified by a redox-recycle loop in which each molecule of  $S_4$  produced by the combined actions of  $E_1$  and  $E_2$  may be sequentially oxidized by  $E_2$  and then reduced at the electrode many times, with additional current being produced in each cycle.

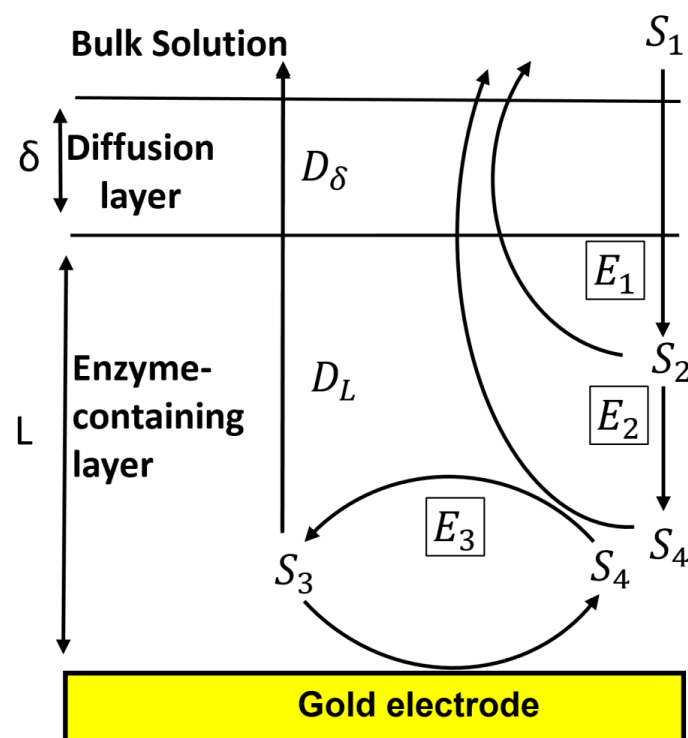


**Figure 1.** Schematic representation of reactions in the IBE biosensor interface.  $S_1$ ,  $S_2$ ,  $S_3$ , and  $S_4$  denote phenylacetate, phenol, catechol, and o-quinone, respectively.  $E_1$ ,  $E_2$ , and  $E_3$  denote acetylcholinesterase, tyrosinase's phenolase activity, and tyrosinase's catecholase activity, respectively.



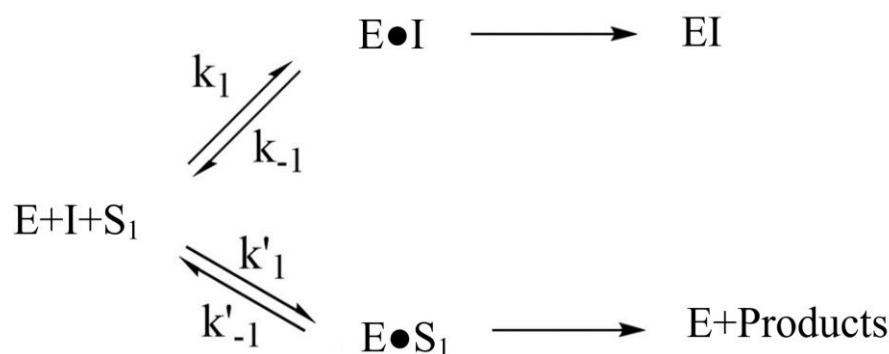


**Figure 4.** Inhibition mechanism of AChE (E) with PMSF (I) in the presence of substrate ( $S_1$ ).

Studies have shown that AChE inhibition with PMSF follows pseudo-first-order kinetics [35] (Equation (1)):

$$\ln \frac{V'_{\max,1}}{V_{\max,1}} = -k't' \quad (1)$$

where  $V_{\max,1}$  and  $V'_{\max,1}$  are the maximum reaction rates for AChE in the absence of the inhibitor and when incubated with inhibitor for a time of  $t'$ , respectively.  $k'$  is the pseudo-first-order rate constant for the inactivation of AChE by PMSF (Equation (2)):

$$k' = \frac{k_2[I]}{\frac{1}{(1-\gamma)}k_I + [I]} \quad (2)$$

The affinity of PMSF for AChE is given by the Michaelis–Menten type constant,  $k_I$  [35]:

$$k_I = \frac{k_{-1} + k_2}{k_{+1}} \quad (3)$$

where  $k_{+1}$  and  $k_{-1}$  are the forward and backward rate constants for the formation of the Michaelis–Menten type complex, and  $k_2$  is the sulfonylation rate constant (Figure 4). The value of  $\gamma$  is given by Equation (4), where  $K_{m,1}$  is the Michaelis–Menten constant for phenylacetate hydrolysis.

$$\gamma = \frac{[S_1]}{[S_1] + K_{m,1}} \quad (4)$$

PMSF competes with phenylacetate for the active site of AChE, thereby changing  $K_{m,1}$  to an the apparent value  $K'_{m,1}$  (Equation (5)) [25].

$$K'_{m,1} = K_{m,1} \left( 1 + \frac{[I]}{k_I} \right) \quad (5)$$

Equations (6)–(8) describe the enzymatic kinetics of AChE in the presence of PMSF, where  $k_{\text{cat},1}$  is the turnover number of AChE for phenylacetate. By assuming that the rate of PMSF (I) consumption equals the rate of enzyme inactivation, Equation (9) was derived to describe the rate of PMSF (I) consumption.

$$v_1 = \frac{V'_{\max,1}[S_1]}{K'_{m,1} + [S_1]} \quad (6)$$

$$V'_{\max,1} = V_{\max,1}e^{-k't} \quad (7)$$

$$V_{\max,1} = k_{\text{cat},1}E_1 \quad (8)$$

$$\frac{dI}{dt} = -k'E_1e^{-k't} \quad (9)$$

### 2.4.2. Tyrosinase Enzyme Kinetics

Tyrosinase exhibits two enzymatic activities: monophenolase activity, which catalyzes the hydroxylation of phenol to produce o-diphenol (catechol) and catecholase activity, which catalyzes the oxidation of catechol to o-quinone. Figure 5 shows the scheme for the two-step oxidation of phenol with tyrosinase.

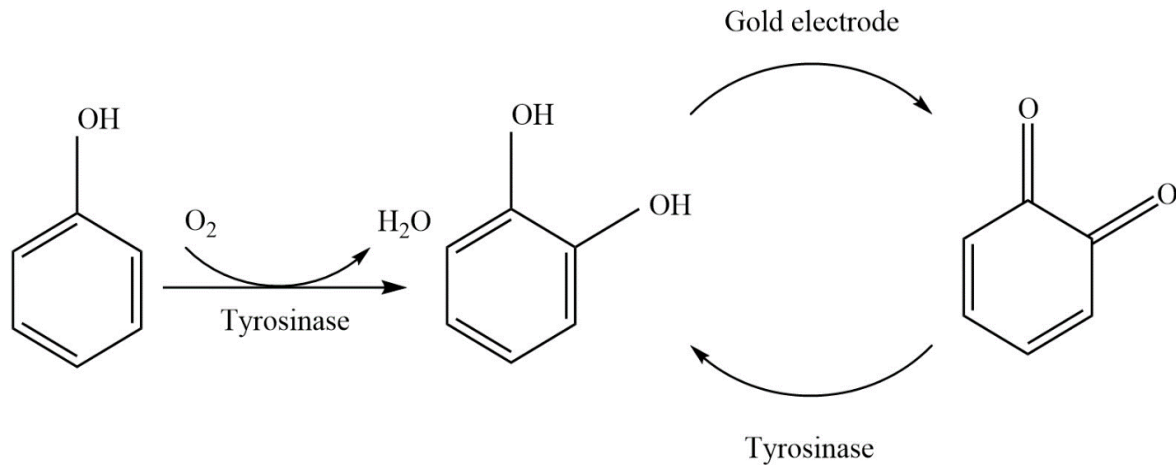


**Figure 5.** Scheme of phenol oxidation with tyrosinase to produce o-quinone.

Studies have shown that the hydroxylation step (monophenolase activity) is much slower than the oxidation step (catecholase activity), and therefore limits the o-quinone production rate [36]. Therefore, we assumed that the rate ( $v_2$ ) of o-quinone ( $S_4$ ) production from phenol ( $S_2$ ) can be obtained from Equations (11)–(12), where  $E_2$  corresponds to phenolase activity of tyrosinase. The rate ( $v_3$ ) of conversion of catechol ( $S_3$ ) to o-quinone ( $S_4$ ) can be given by Equations (12) and (13), where  $E_3$  denotes the catecholase activity of tyrosinase [29]

$$v_2 = \frac{V_{\max,2}[S_2]}{K_{m,2} + [S_2]} \quad (10)$$

$$V_{\max,2} = k_{\text{cat},2} E_2 \quad (11)$$

$$v_3 = \frac{V_{\max,3}[S_3]}{K_{m,3} + [S_3]} \quad (12)$$

$$V_{\max,3} = k_{\text{cat},3} E_3 \quad (13)$$

The molecules of o-quinone produced by tyrosinase are assumed to be reduced back to catechol at the working electrode at a rate described by the Butler–Volmer equation (Equation (14)):

$$J = nFD_L \left[ \frac{\partial Q}{\partial x} \right]_{x=0} = nFK_0[Q]_{x=0} e^{\left( -\frac{\alpha nF(E-E_h)}{RT} \right)} - nFK_0[C]_{x=0} e^{\left( \frac{(1-\alpha)nF(E-E_h)}{RT} \right)} \quad (14)$$

where  $J$  is the electric current density,  $n$  is the number of electrons transferred (e.g.,  $n = 2$  for the electrochemical reduction of  $Q$ ),  $\alpha$  is the charge transfer coefficient (assumed to be 0.4),  $F$  is the Faraday constant ( $96,485 \text{ C mol}^{-1}$ ),  $K_0$  is the apparent electron transfer rate constant for  $Q$ ,  $R$  is the universal gas constant ( $8.314 \text{ J K}^{-1} \text{ mol}^{-1}$ ),  $T$  is the absolute temperature (298 K), and  $E_h$  is the redox potential for electrochemical reduction of  $Q$  to  $C$  under the experimental conditions. An  $E_h$  value of 0.15 V was determined as the midpoint between the cathodic peak and anodic peak of cyclic voltammogram obtained under the same conditions.

### 2.4.3. Mass Balance Equations

The mass balance equations including diffusion and enzymatic reaction for  $S_1$ ,  $S_2$ ,  $S_3$ ,  $S_4$ , and  $I$  across the enzyme-containing layer ( $0 < x < L$ ) can be derived (Equations (15)–(19)).

$$\frac{\partial S_1}{\partial t} = D_L \frac{\partial^2 S_1}{\partial x^2} - \frac{V'_{\max,1}[S_1]}{K'_{m,1} + [S_1]} \quad (15)$$

$$\frac{\partial S_2}{\partial t} = D_L \frac{\partial^2 S_2}{\partial x^2} - \frac{V_{\max,2}E_2[S_2]}{K_{m,2} + [S_2]} + \frac{V'_{\max}[S_1]}{K'_{m,1} + [S_1]} \quad (16)$$

$$\frac{\partial S_3}{\partial t} = D_L \frac{\partial^2 S_3}{\partial x^2} - \frac{V_{\max,3}E_3[S_3]}{K_{m,3} + [S_3]} \quad (17)$$

$$\frac{\partial S_4}{\partial t} = D_L \frac{\partial^2 S_4}{\partial x^2} + \frac{V_{\max,3}[S_3]}{K_{m,3} + [S_3]} \quad (18)$$

$$\frac{\partial I}{\partial t} = D_L \frac{\partial^2 I}{\partial x^2} + k'E_1e^{-k't} \quad (19)$$

### 2.4.4. Boundary Conditions

Because Q reduction at the electrode generates C in equimolar amounts, the fluxes of Q and C at  $x = 0$  were assumed to be equal in magnitude but opposite in sign (Equation (20)).

$$D_L \left[ \frac{\partial S_4}{\partial x} \right]_{x=0} = -D_L \left[ \frac{\partial S_3}{\partial x} \right]_{x=0} \quad (20)$$

At  $x = 0$ ,  $S_1$ ,  $S_2$ ,  $S_3$ , and  $I$  are assumed not to be consumed or produced at the electrode (Equation (21)):

$$\left[ \frac{\partial S_1}{\partial x} \right]_{x=0} = 0, \left[ \frac{\partial S_2}{\partial x} \right]_{x=0} = 0, \left[ \frac{\partial S_3}{\partial x} \right]_{x=0} = 0, \left[ \frac{\partial I}{\partial x} \right]_{x=0} = 0 \quad (21)$$

Partitioning kinetics of all reactants were assumed to be rapid enough that the interfacial concentrations at the boundaries of the diffusion layer and enzyme-containing layer remained at equilibrium. Identical partition coefficients ( $k_p = 1$ ) were assumed for all reactants (Equations (22)–(26)).

$$[S_1]_{L+} = k_p [S_1]_{L+} \quad (22)$$

$$[S_2]_{L+} = k_p [S_2]_{L+} \quad (23)$$

$$[S_3]_{L+} = k_p [S_3]_{L+} \quad (24)$$

$$[S_4]_{L+} = k_p [S_4]_{L+} \quad (25)$$

$$[I]_{L+} = k_p [I]_{L+} \quad (26)$$

The bulk solution (where  $x = \infty$ ) contained  $S_1$  at a concentration of  $S_1(\infty)$  but negligible concentrations of  $S_2$ ,  $S_3$ , and  $S_4$  (Equations (27)–(31)).

$$[S_1]_{x=\infty} = C(\infty) \quad (27)$$

$$[S_2]_{x=\infty} = 0 \quad (28)$$

$$[S_3]_{x=\infty} = 0 \quad (29)$$

$$[S_4]_{x=\infty} = 0 \quad (30)$$

$$[I]_{x=\infty, t < T_0} = 0, [I]_{x=\infty, T_0 < t} = I(\infty) \quad (31)$$

Because no reaction is assumed to occur in the diffusion layer, the flux of species entering this layer was assumed to equal that exiting it (Equations (32)–(36)).

$$D_L \left[ \frac{\partial S_1}{\partial x} \right]_{x=L-} = \frac{D_\delta}{k_p \delta} \{ k_p S_1(\infty) - [S_1]_{x=L-} \} \quad (32)$$

$$D_L \left[ \frac{\partial S_2}{\partial x} \right]_{x=L-} = -\frac{D_\delta}{\delta} \{ [S_2]_{x=L+} - 0 \} = -\frac{D_\delta}{k_p \delta} [S_2]_{x=L-} \quad (33)$$

$$D_L \left[ \frac{\partial S_3}{\partial x} \right]_{x=L-} = -\frac{D_\delta}{\delta} \{ [S_3]_{x=L+} - 0 \} = -\frac{D_\delta}{k_p \delta} [S_3]_{x=L-} \quad (34)$$

$$D_L \left[ \frac{\partial S_4}{\partial x} \right]_{x=L-} = -\frac{D_\delta}{\delta} \{ [S_4]_{x=L+} - 0 \} = -\frac{D_\delta}{k_p \delta} [S_4]_{x=L-} \quad (35)$$

$$D_L \left[ \frac{\partial I}{\partial x} \right]_{x=L-} = \frac{D_\delta}{k_p \delta} \{ k_p I(\infty) - [I]_{x=L-} \} \quad (36)$$

#### 2.4.5. Initial Conditions

Initial conditions of phenylacetate at injection time ( $t = 0$ ) are given in Equation (37):

$$[S_i]_{i=2,4,0 \leq x \leq L} = 0, [S_1]_{0 \leq x < L} = 0, [S_1]_{x=L} = S_1(\infty) \quad (37)$$

The inhibitor concentration ( $I$ ) was assumed to be zero before it was injected at ( $T_0$ ) and was assumed to be constant throughout the enzyme-containing layer and solution afterward (Equation (38)):

$$[I]_{0 < t < T_0} = 0, [I]_{T_0 < t} = I(\infty) \quad (38)$$

A splitting-finite-difference algorithm was programmed in MATLAB and used to solve the mass balance equations (Equations (15)–(19)) numerically using the parameters given in Table 1 and the boundary and initial conditions given in Equations (20)–(38).

**Table 1.** Parameters and variables used in the numerical simulation.

Parameter/Variable	Dimensional Parameter	Variation Range	Value Used to Fit Experimental Data
Time	$t$ , s	0–300	–
Distance from electrode surface	$x$ , cm	$3.0 \times 10^{-4}$ – $3.0 \times 10^{-2}$	$3.0 \times 10^{-3}$
Phenylacetate concentration	( $S_1$ ), mM	0–1.5	0.9
PMSF concentration	( $I$ ), mM	0–0.5	–
Acetylcholinesterase concentration	( $E_1$ ), $\mu$ M	0–100	30
Tyrosinase Concentration (phenolase activity)	( $E_2$ ), mM	0–5	1.45
Tyrosinase Concentration (catecholase activity)	( $E_3$ ), mM	0–5	1.65
Michaelis–Menten constant of phenylacetate	$K_{m,1}$ , $\mu$ M	0–100	50.5
Michaelis–Menten constant of phenol	$K_{m,2}$ , $\mu$ M	0–10	0.25
Michaelis–Menten constant of catechol	$K_{m,3}$ , $\mu$ M	0–10	0.22
Acetylcholinesterase turnover number for phenylacetate	$k_{cat,1}$ , $s^{-1}$	$2.0 \times 10^2$ – $2.0 \times 10^5$	$2.3 \times 10^4$
Tyrosinase turnover number for phenol	$k_{cat,2}$ , $s^{-1}$	$2.0$ – $2.0 \times 10^3$	20
Tyrosinase turnover number for catechol	$k_{cat,3}$ , $s^{-1}$	$2.0$ – $2.0 \times 10^3$	760
Dissociation constant of PMSF	$k_I$ , mM	0.02–2.0	0.25

Table 1. Cont.

Parameter/Variable	Dimensional Parameter	Variation Range	Value Used to Fit Experimental Data
Reaction constant of deactivation of acetylcholinesterase with PMSF	$k_2, s^{-1}$	0.001–0.1	0.005
Enzyme-containing layer thickness	$L, nm$	10–100	25
Diffusion layer thickness	$\delta, \mu m$	10–200	30
Diffusion coefficient in diffusion layer	$D_\delta, cm^2 s^{-1}$	$1 \times 10^{-6}$ – $9 \times 10^{-5}$	$2.2 \times 10^{-5}$
Diffusion coefficient in enzyme-containing layer	$D_L, cm^2 s^{-1}$	$1 \times 10^{-8}$ – $9 \times 10^{-6}$	$2.28 \times 10^{-8}$
Standard redox electrochemical potential of O-quinone	$E^0, V$	0.15	0.15
Heterogeneous electron transfer rate constant	$K_0, cm s^{-1}$	$1 \times 10^{-7}$ – $1 \times 10^{-4}$	$1 \times 10^{-5}$

### 3. Results and Discussion

#### 3.1. Biosensor's Response to PMSF

Figure 6 shows a typical amperometry experiment to detect PMSF. Phenylacetate was added at about 35 s, and PMSF was added at about 190 s. As soon as a buffer sample containing PMSF was added, the biosensor's current rapidly declined and then returned to a relatively stable value whose magnitude varied with the PMSF concentration in the sample. A first-order time constant for the IBE biosensors' response to PMSF (defined as 63% toward the relatively stable current value) was typically about 20 s.

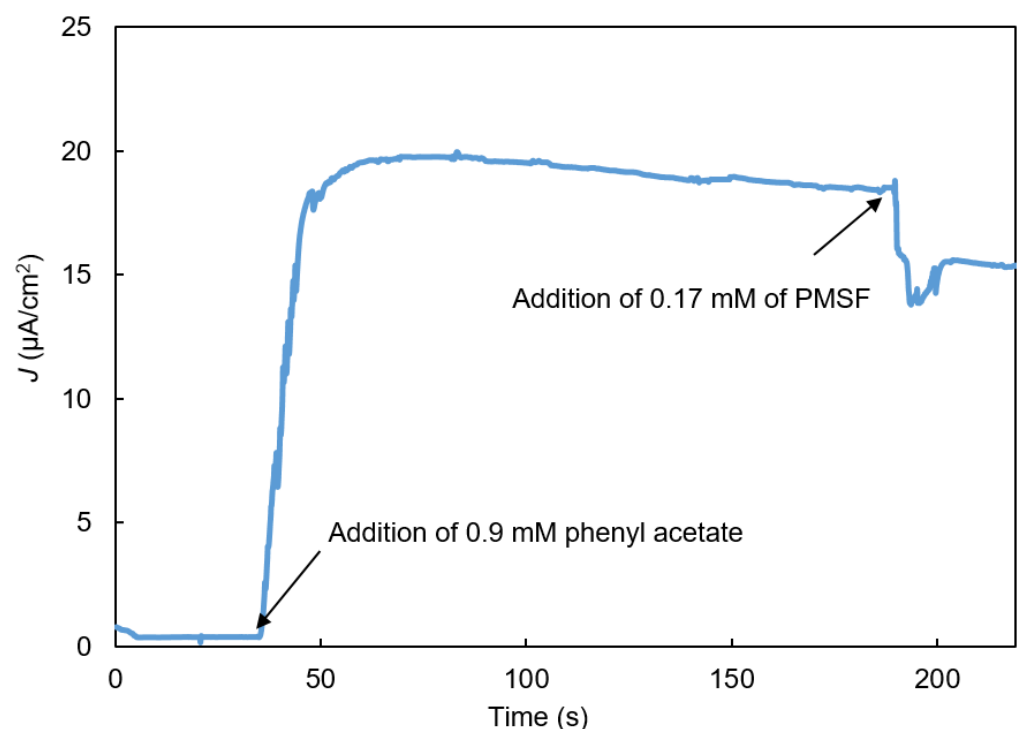


**Figure 6.** Current vs. time response of the bi-enzyme biosensor to the addition of phenylacetate ( $S_1$ ) to obtain a final phenylacetate ( $S_1$ ) concentration of 0.9 mM followed by the addition of inhibitor PMSF to obtain a final PMSF concentration of 0.17 mM.

Control experiments were conducted to characterize the IBE biosensor's response to blank samples with the addition of a bolus of the buffer without PMSF (Figure 7). As soon as a buffer sample without PMSF was added, the biosensor's signal rapidly declined and

then returned to a relatively stable current very close to that before the blank sample was added.

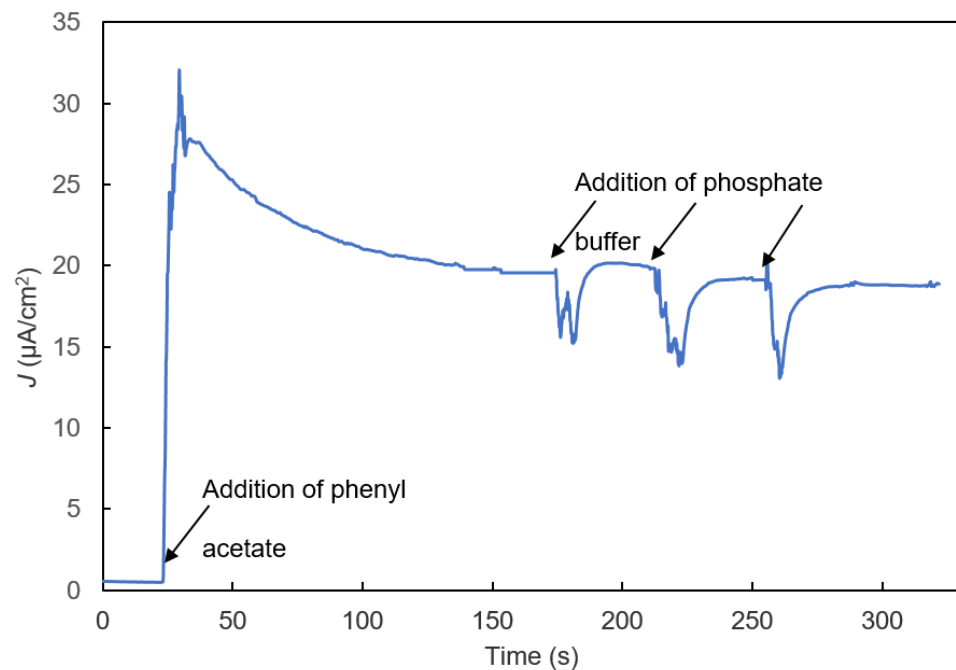


**Figure 7.** Control experiment to study the effect of phosphate buffer addition on the bi-enzyme biosensor's signal.

The PMSF-challenge experiments described above were repeated for samples containing a variety of PMSF concentrations. Figure 8 shows the current to which the signal returned after the initial decline as a function of the PMSF concentration in the sample. The calibration curve had a sensitivity (slope) of  $18.4 \mu\text{A cm}^{-2} (\text{mM PMSF})^{-1}$  and an  $R^2$  value for a linear fit of 0.995.

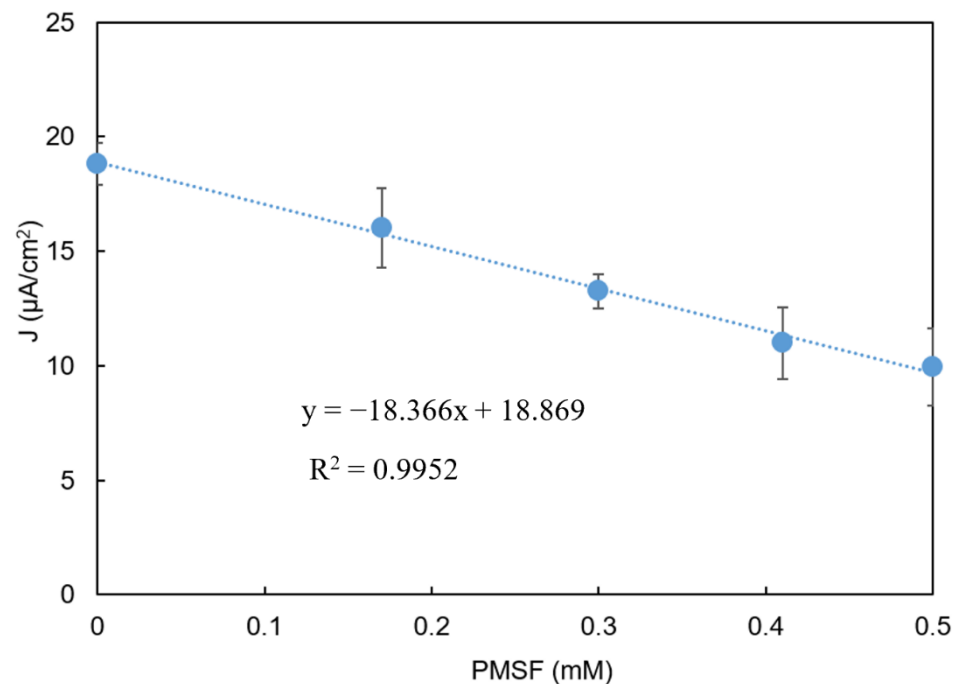


**Figure 8.** Current vs. PMSF concentration. Error bars indicate the mean  $\pm$  standard deviation of three replicates. Phenylacetate: 0.9 mM.  $y = -18.366x + 18.869$ ,  $R^2 = 0.9952$ .

### 3.2. Validation of the Mathematical Model and Simulation of the Biosensor's Response

The numerical model successfully simulated the biosensor's behavior shown in Figures 6–8. To explain the initial, rapid signal decline triggered by sample addition, we hypothesized that the increase in convective mass transfer while the sample was being pipetted into the solution on the SPE altered the pseudo-steady-state concentration gradients of the reacting chemical intermediates ( $S_2$ ,  $S_3$ , and  $S_4$ ) in the enzyme-containing layer. To simulate this effect in the model, we decreased the concentrations of these intermediates in the enzyme-containing layer by some fraction (e.g., 20%) at  $t = T_0$  (Equations (39)–(41)):

$$[S_2]_{0 < x < L, t = T_0^+} = 0.8 [S_2]_{0 < x < L, t = T_0^-} \quad (39)$$

$$[S_3]_{0 < x < L, t = T_0^+} = 0.8 [S_3]_{0 < x < L, t = T_0^-} \quad (40)$$

$$[S_4]_{0 < x < L, t = T_0^+} = 0.8 [S_4]_{0 < x < L, t = T_0^-} \quad (41)$$

This change enabled the model to predict the biosensors observed dynamics following sample addition, including the sudden drop in the biosensor's signal, followed by a return to a stable current (Figure 9A), providing support for the hypothesis.

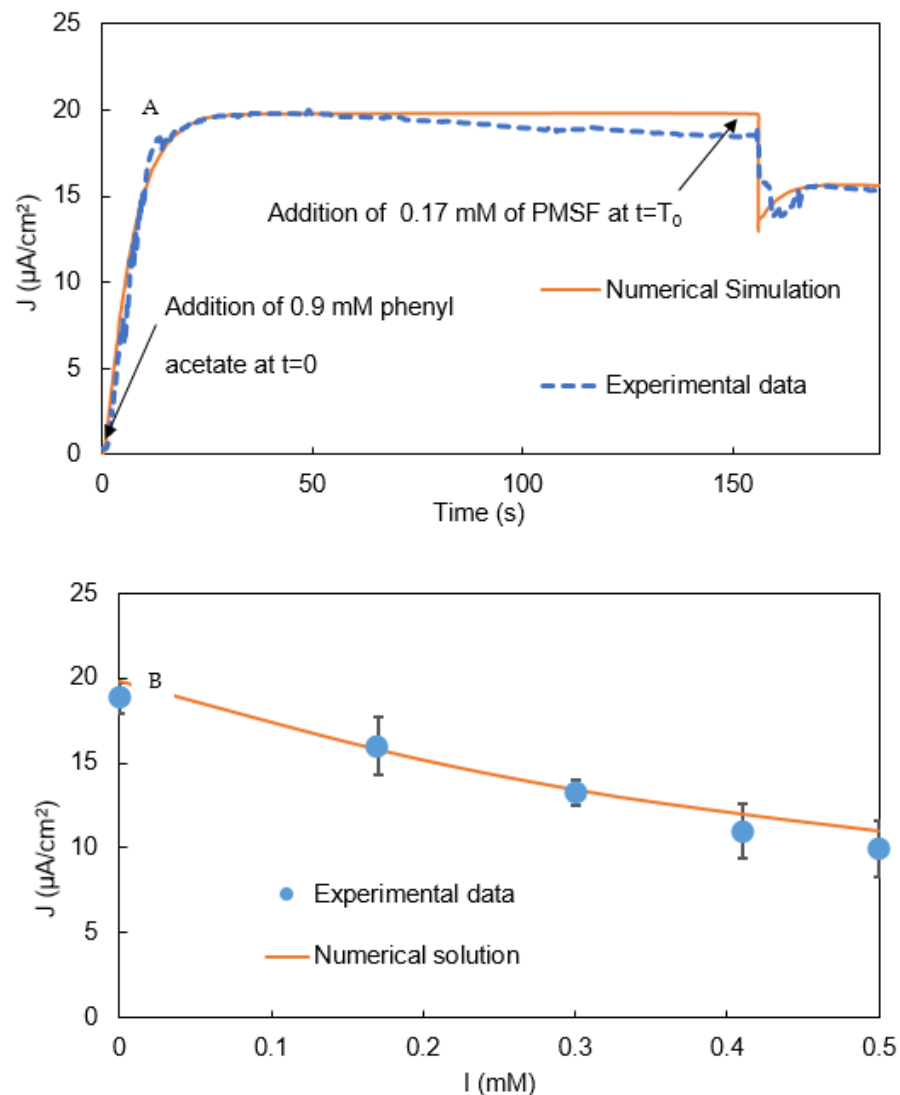


**Figure 9.** (A): Simulated the bi-enzyme biosensor's signal vs. time. (B): Simulated current density vs. PMSF concentration ( $I$ ). Error bars indicate the mean  $\pm$  standard deviation of three replicates.

The model was also able to accurately predict the relatively stable current that resulted after the initial biosensor-response dynamics as a function of the PMSF concentration in the sample (Figure 9B).

Figures 6, 7 and 9B show that after phenylacetate was added, the biosensor's current increased rapidly, went through a maximum, and then exhibited a gradual decay. The mechanism responsible for the decay is unknown, but it may result from the formation of byproducts of o-quinone reduction at the electrode that are not re-oxidized as rapidly by tyrosinase as catechol. The result of such a reaction would be a gradual increase in the byproduct concentration, and decrease in the catechol and o-quinone concentrations, and, consequently, a gradual decrease in the biosensor's current.

### Signal Amplification by Redox-Recycle Loop

The degree of biosensor signal amplification due to the redox-recycle loop involving catechol and O-quinone (Figure 5) activity can be quantified using an amplification factor (AF), which is defined as the ratio of the biosensor's current density (J) in the presence of catecholase activity to that in the absence of the catecholase activity (Equation (42)) [29]:

$$AF = \frac{J|_{E_3 \neq 0}}{J|_{E_3 = 0}} \quad (42)$$

After validating the biosensor model (Figure 9A,B), we used it to explore the extent of signal amplification under a variety of operating conditions. Figure 10A shows the model-predicted output current both in the presence and absence of the amplification system. To predict the absence of amplification system zero, catecholase activity of tyrosinase was set to zero in the model. The predicted AF of about three across the range of [I] simulated indicates that redox amplification increases the biosensor's current roughly three-fold under the experimental conditions.

The effect of catecholase concentration (E3) on the predicted AF was also explored with the model (Figure 10B). This result shows an increasing tyrosinase concentration would increase the biosensor's output by increasing the redox amplification.

### 3.3. Biosensor Sensitivity

Biosensor sensitivity (S) with respect to PMSF concentration [I] is defined in Equation (43):

$$S = \frac{dJ}{d[I]} \quad (43)$$

To calculate S for a given set of experimental conditions, the incremental change in J ( $\Delta J$ ) resulting from an incremental change in [I] ( $\Delta[I]$ ) was calculated by the model. Then the asymptotic value of the ratio  $\Delta J/\Delta[I]$  as  $\Delta[I]$  approached zero was determined and used as the S value for those conditions. The resulting S values were plotted as function of a dimensionless phenylacetate concentration ( $[S_1]/K_{m,1,app}$ ) for several [I] values (Figure 11A).

All the sensitivity curves exhibited a maximum value for the following reasons. At low  $[S_1]/K_{m,1,app}$  values, the  $S_1$  hydrolysis rate, and thus the J value, is so low that the maximum possible drop in J due to an increase on PMSF concentration is also small. At large  $[S_1]/K_{m,1,app}$  values, almost all AChE active sites are occupied with  $S_1$  values, and are unavailable to bind to PMSF molecules; thus the addition of PMSF has little effect on J.

For all  $[S_1]/K_{m,1,app}$  values shown, sensitivity values increased as the PMSF concentration decreased. The lower the PMSF concentration, the higher the  $S_1$  hydrolysis rate, the J value, and the maximum possible drop in J as the PMSF concentration is increased.

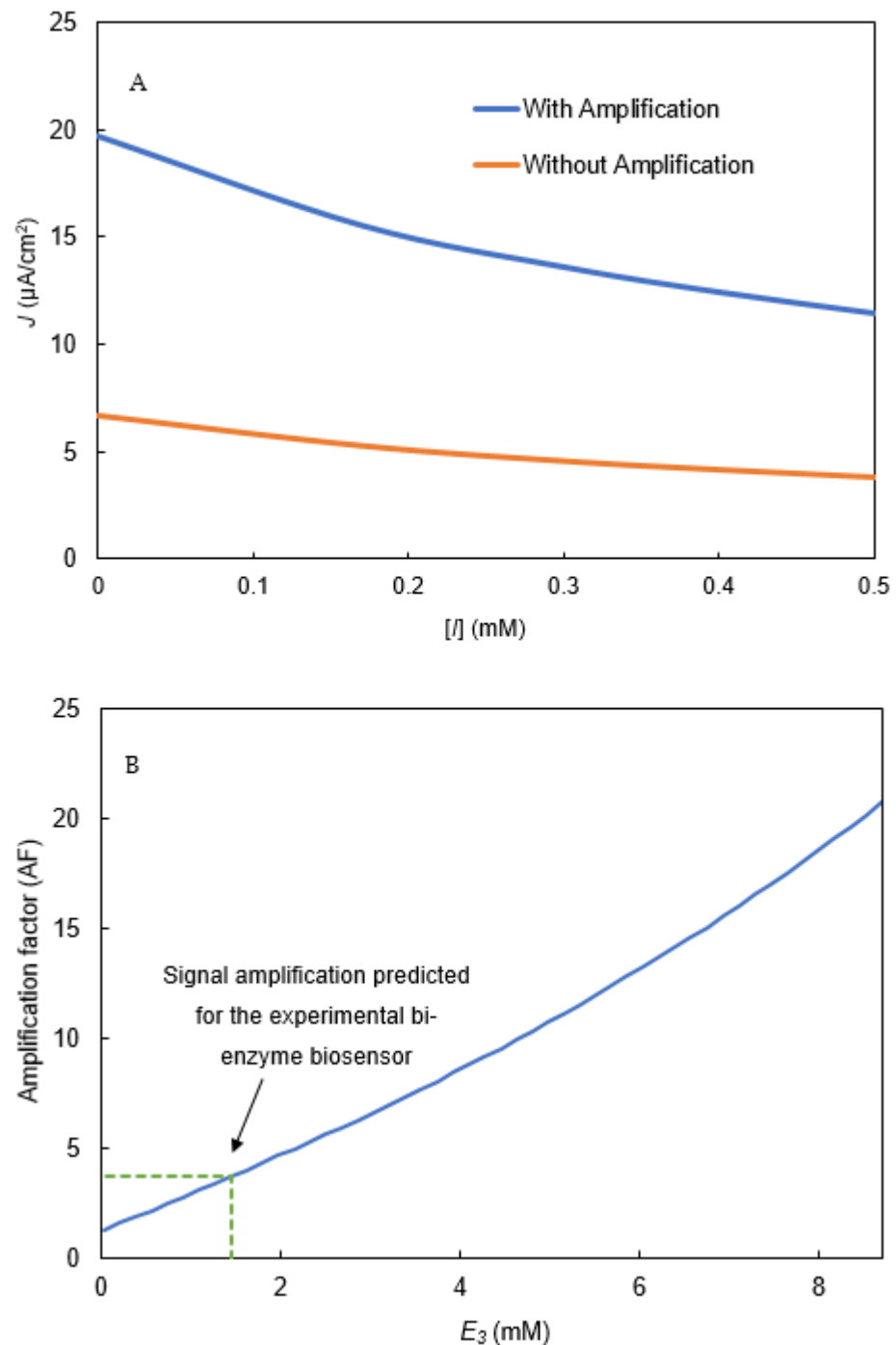


**Figure 10.** (A): Simulated current density with and without ( $E_3 = 0$ ) the amplification system in the bi-enzyme biosensor. (B): Signal amplification in bi-enzyme biosensor due to  $S_3$  recycling caused by catecholase activity ( $E_3$ ).

The calculated  $S$  values were also plotted as a function of dimensionless AChE concentration for several dimensionless tyrosinase concentrations (Figure 11B).

For all tyrosinase concentrations, plots of sensitivity vs.  $(\text{AChE})/(\text{AChE}^*)$  exhibited a maximum. At low  $[\text{AChE}]/[\text{AChE}^*]$  values, they are equal to the  $S_1$  hydrolysis rate, and thus the  $J$  value is so low that the  $[\text{AChE}]/[\text{AChE}^*]$  values are different from the  $S_1$  hydrolysis limits,  $J$ ; therefore, the inhibition of AChE by PMSF addition has little effect on  $J$ .

For all of the  $[\text{AChE}]/[\text{AChE}^*]$  values shown, sensitivity values increased as the tyrosinase concentration increased. This effect is attributed to the catecholase activity,

and thus greater amplification and  $J$  values that occur at higher tyrosinase concentrations (Figure 11B).

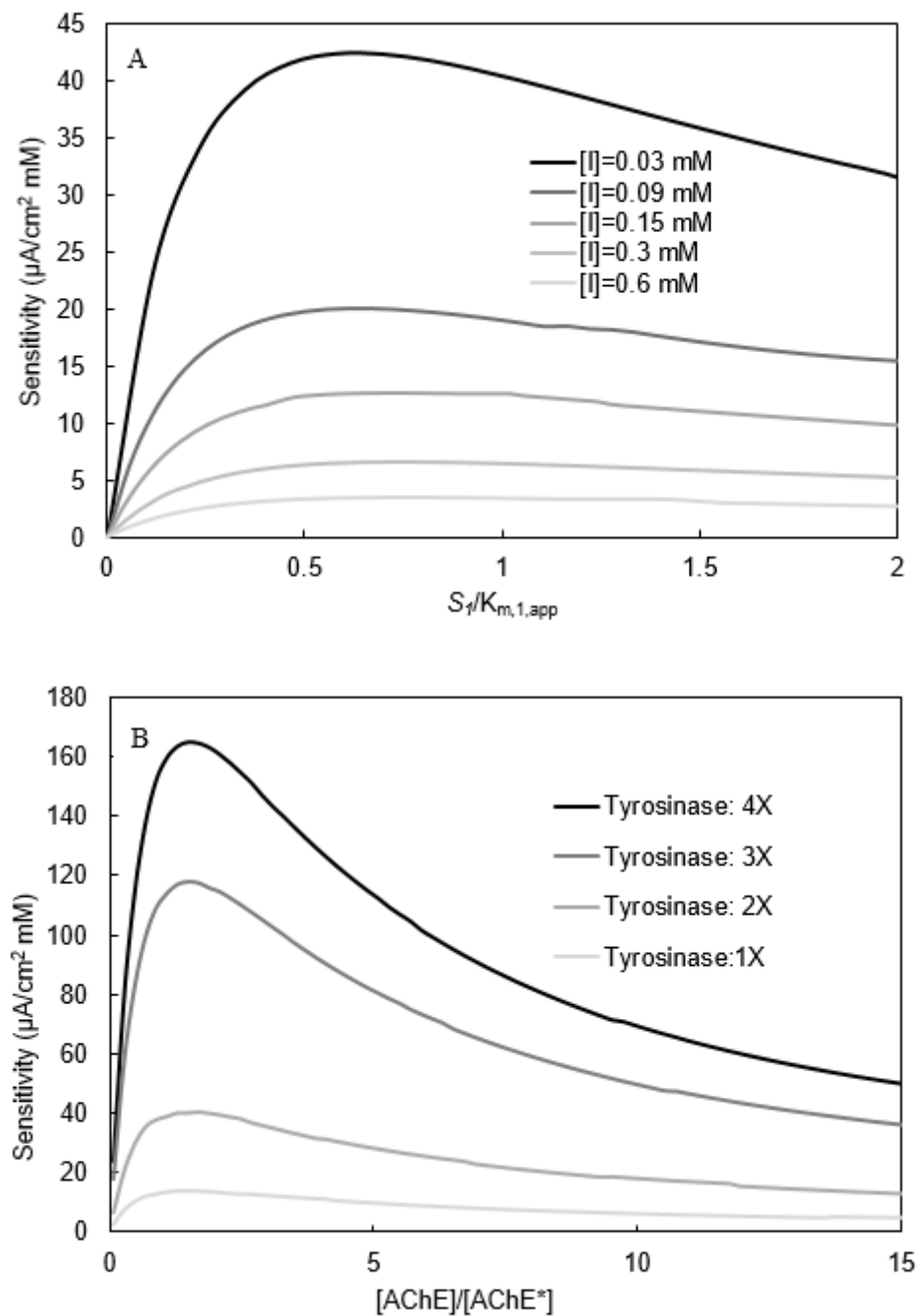


**Figure 11.** (A): Sensitivity vs. phenylacetate concentration ( $S_1$ ).  $S_1$  has been normalized with  $K_{m,1,app}$ . (B): Sensitivity vs.  $[\text{AChE}]$  at different tyrosinase concentrations.  $[\text{AChE}]$  has been normalized with  $[\text{AChE}^*] = 3 \mu\text{M}$ .  $[I] = 0.3 \text{ mM}$ .

### 3.4. Identification of Rate Limiting Step

In a recent publication, we described the use of dimensionless groups to assess the rate-limiting step(s) in amperometric biosensors. The biosensor's current results from the interplay of multiple mass transfer and reaction steps, each of which has the potential to be rate-limiting (i.e., control the biosensor current output) to some extent. Because the mechanistic model predicts the rate of each step, it enables the extent to which each step is rate-limiting to be calculated.

We used Equation (44) and parameter values from Table 1 to calculate the Damkohler number ( $\sigma$ ), defined as the square root of the dimensionless ratio of the relative rates of enzymatic reaction ( $\frac{V_{\max}}{K_M}$ ) and diffusional mass transfer ( $\frac{D_L}{L^2}$ ) within the enzyme-containing layer [37].

$$\sigma^2 = \frac{V_{\max}L^2}{D_LK_M} \quad (44)$$

The  $\sigma$  values for AChE and tyrosinase were in the order of  $10^{-5}$ , indicating that the diffusion steps are many orders of magnitude faster than the reaction steps [32,38].

Flux-control analysis has been used to determine the extent to which the rates of individual enzymatic reactions limit the overall mass flux through a metabolic pathway [39]. We extended this approach to assess to what extent both individual enzymatic reactions and electrochemical reactions limited current production by the biosensor. We defined a current-control coefficient ( $C_{V_i}^J$ ) for a given reaction step ( $V_i$ ) as the ratio of the percent change in the biosensor's output current ( $J$ ) to the percent change in a given  $V_i$  while holding all other independent variables constant (Equation (45)). We used the validated model to calculate  $C_{V_i}^J$  values for each of the three reaction rates involved in generating that current: the AChE reaction rate ( $V_1$ ), the tyrosinase reaction rate ( $V_2$ ), or the electrochemical reaction rate ( $V_3$ ). The mechanistic model allowed the enzymatic reaction rates ( $V_1$  and  $V_2$ ) to be varied by adjusting the assumed AChE and tyrosinase concentrations, respectively, and the electrochemical reaction rate ( $V_3$ ) to be varied by adjusting the assumed working-electrode overpotential ( $E-E_h$ ). Figure 12A–C show calculated  $C_{V_1}^J$  values as a function of the AChE concentration,  $C_{V_2}^J$  values as a function of the tyrosinase concentration, and  $C_{V_3}^J$  values as a function of overpotential ( $E-E_h$ ), respectively.

Figure 12A shows the effect of normalized AChE concentration  $C_{V_1}^J$  values. The curve declines monotonically from a value of 1 as the AChE concentration increases. For the AChE concentration used in the validated biosensor mathematical model ( $3 \mu\text{M}$ ), a current-control coefficient of 0.52 is predicted.

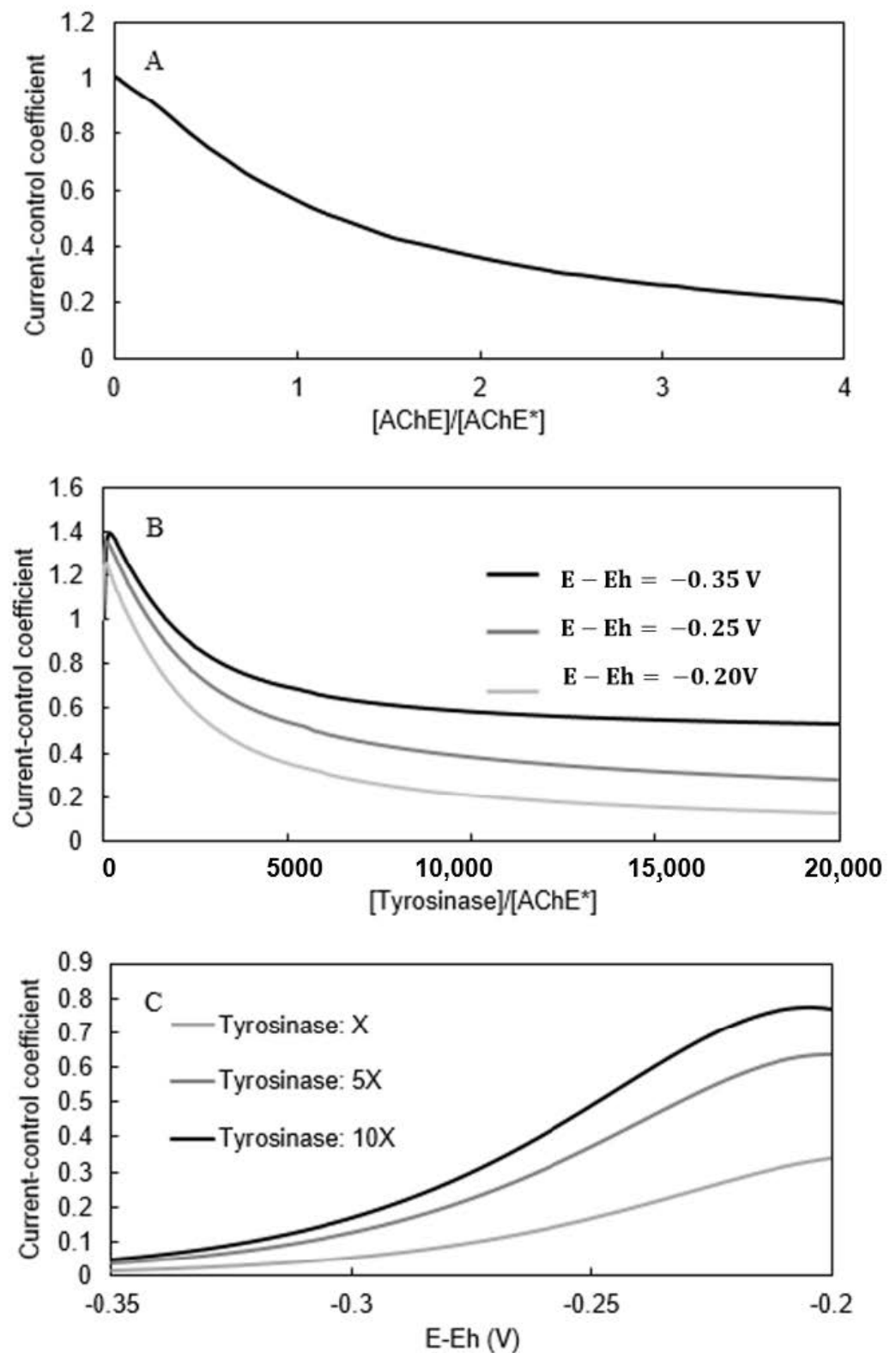
$$\frac{dJ}{J} / \frac{dV_i}{V_i} = C_{V_i}^J \quad (45)$$

Figure 12B shows the effect of tyrosinase concentration (normalized by a constant [AChE] value of  $3 \mu\text{M}$ ) on  $C_{V_2}^J$  values. The curve exhibits a maximum at very low tyrosinase concentrations and then declines monotonically as the tyrosinase concentration increases. Similar curve shapes were predicted for three applied working-electrode overpotentials, with  $C_{V_i}^J$  values increasing as the overpotential increases in magnitude (i.e., the working electrode becomes more negative).

Figure 12C shows the effect of applied overpotential on  $C_{V_3}^J$  values appear to decrease monotonically from a maximum value as overpotential values increase in magnitude (i.e., the working electrode becomes more negative). Similar curve shapes were predicted for the three tyrosinase concentrations studied, with  $C_{V_3}^J$  values increasing as the tyrosinase concentration increases.

Once validated, the IBE model's predictive power has utility for guiding future biosensor design and optimization efforts. For example, Figure 8 indicates that the IBE biosensor has a sensitivity for detecting PMSF of  $18.4 \mu\text{A cm}^{-2} (\text{mM PMSF})^{-1}$ . To increase that sensitivity, researchers might consider whether it would be possible to increase the percent change in biosensor output per percent change in AChE activity due to PMSF inhibition (i.e., increase  $C_{V_1}^J$ ). Figure 12A predicts that the  $C_{V_1}^J$  value under the experimental conditions was 0.52, and that the  $C_{V_1}^J$  value could be increased by about a factor of two by decreasing the AChE concentration. The potential utility of other strategies to increase the sensitivity could be evaluated quickly and inexpensively *in silico* using the model. For example, the effects of changing the thickness of the enzyme-containing layer, the

concentrations and ratios of the two enzymes, the working electrode's overpotential on the sensitivity could be rapidly assessed using the model.



**Figure 12.** (A): Current-control coefficient vs.  $[AChE]/[AChE^*]$ . (B): Current-control coefficient for tyrosinase. Tyrosinase concentration was normalized using  $[AChE^*] = 3 \mu M$ . (C): Current-control coefficient based on the electrochemical reaction vs. working-electrode overpotential ( $E - E_h$ ).

#### 4. Conclusions

This study demonstrated the utility of a novel experimental and modeling framework to characterize and optimize IBE electrochemical biosensors to detect markers of neurological diseases (e.g., inhibitors of neural esterases). The experimental system was an amperometric biosensor with an oxidase (tyrosinase) and a neural esterase (AChE) co-immobilized on the working electrode of a commercially available SPE array to detect markers of neurological disease. The mechanistic model included a system of coupled, partial-differential, mass-balance equations that described the simultaneous reaction and diffusion of reactants and products between the bulk solution, the enzyme-containing layer, and the working electrode. These equations, together with their boundary and initial conditions, were solved numerically using a splitting-finite-difference algorithm. The model was able to reproduce several trends in the experimental results, including a steady-state biosensor current as a function of the inhibitor (PMSF) concentration, as well as unsteady-state dynamics of the biosensor current following the addition of a reactant (phenylacetate) and an ACE inhibitor (PMSF).

The successful application of our integrated experimental and modeling framework in this paper for IBE biosensors and in a previous paper for a novel amperometric electrochemical immunosensor [26] has demonstrated that the approach is generic and has wide utility for mechanistic modeling of the key mass-transfer and reaction steps that determine the biosensor's amplitude and sensitivity. Moreover, the novel dimensional-analysis approach (e.g., current-control coefficients, sensitivity coefficients, and Damkohler numbers) has been shown to be capable of determining the degree to which various steps limit the biosensor's signal magnitude and sensitivity to the target analyte. These capabilities enable the framework to be used for *in silico* design of biosensors having performance properties that are customized for the target application, whether that might be the maximum sensitivity at low analyte concentrations or a linear response over a very wide analyte range. The framework can also predict which independent variable(s) (e.g., the thickness of the enzyme-containing layer, the concentrations and ratios of the two enzymes, the working electrode's overpotential) would be most effective in obtaining the desired dependent performance variable(s) (e.g., signal magnitude, analyte sensitivity). Finally, this paper's extension of the modeling capability to predict unsteady-state IBE biosensor responses provides a novel capability to design biosensors having desired dynamic properties, thereby providing the capability for a new dimension of experimental characterization using electrochemical biosensors.

**Author Contributions:** Conceptualization, N.R., R.M.W., and P.S.; methodology, N.R., R.M.W., and P.S.; software, N.R.; validation, N.R., R.M.W., and P.S. formal analysis, N.R., R.M.W., and P.S.; investigation, N.R., R.M.W., and P.S.; resources, N.R., R.M.W., and P.S.; data curation, N.R.; writing—original draft preparation, N.R. and R.M.W.; writing—review and editing, N.R., R.M.W., and P.S.; supervision, R.M.W.; project administration, R.M.W.; funding acquisition, R.M.W. All authors have read and agreed to the published version of the manuscript.

**Funding:** This material is based on work supported by the National Science Foundation under Grant No. 1444991, a Michigan State University MTRAC for the Bio-Economy grant, and a grant from the USDA National Institute of Food and Agriculture (Hatch project 1018025).

**Institutional Review Board Statement:** Not applicable.

**Informed Consent Statement:** Not applicable.

**Data Availability Statement:** Not applicable.

**Acknowledgments:** We gratefully acknowledge Matthew Musho and Jeff Culver of Conductive Technologies Incorporated (CTI) for their helpful discussions and donation of CTI electrode arrays for research related to this project. We also gratefully acknowledge Mohsen Zayernouri in the MSU's Computational Mathematics, Science, and Engineering Department for his assistance in developing the splitting-finite-difference algorithm and Marissa Beatty, Kelly Potts, and Patrick Goughler for their participation in the research while they were undergraduate research assistants at MSU.

**Conflicts of Interest:** The authors declare no conflict of interest.

## References

1. Zhang, S.; Wright, G.; Yang, Y. Materials and techniques for electrochemical biosensor design and construction. *Biosens. Bioelectron.* **2000**, *15*, 273–282. [[CrossRef](#)]
2. Uniyal, S.; Sharma, R.K. Technological advancement in electrochemical biosensor based detection of Organophosphate pesticide chlorpyrifos in the environment: A review of status and prospects. *Biosens. Bioelectron.* **2018**, *116*, 37–50. [[CrossRef](#)]
3. Kucherenko, I.; Soldatkin, O.; Dzyadevych, S.; Soldatkin, A. Electrochemical biosensors based on multienzyme systems: Main groups, advantages and limitations—A review. *Anal. Chim. Acta* **2020**, *1111*, 114–131. [[CrossRef](#)]
4. Ronkainen, N.J.; Halsall, H.B.; Heineman, W.R. Electrochemical biosensors. *Chem. Soc. Rev.* **2010**, *39*, 1747–1763. [[CrossRef](#)]
5. Menon, S.; Mathew, M.R.; Sam, S.; Keerthi, K.; Kumar, K.G. Recent advances and challenges in electrochemical biosensors for emerging and re-emerging infectious diseases. *J. Electroanal. Chem.* **2020**, *878*, 114596. [[CrossRef](#)]
6. Grieshaber, D.; MacKenzie, R.; Vörös, J.; Reimhult, E. Electrochemical biosensors—Sensor principles and architectures. *Sensors* **2008**, *8*, 1400–1458. [[CrossRef](#)]
7. Gerard, M.; Chaubey, A.; Malhotra, B. Application of conducting polymers to biosensors. *Biosens. Bioelectron.* **2002**, *17*, 345–359. [[CrossRef](#)]
8. Worsfold, P.; Townshend, A.; Poole, C.F.; Miró, M. *Encyclopedia of Analytical Science*; Elsevier: Amsterdam, The Netherlands, 2019.
9. Meena, A.; Rajendran, L. Mathematical modeling of amperometric and potentiometric biosensors and system of non-linear equations—Homotopy perturbation approach. *J. Electroanal. Chem.* **2010**, *644*, 50–59. [[CrossRef](#)]
10. Honeychurch, K.C.; Piano, M. Electrochemical (bio) sensors for environmental and food analyses. *Biosensors* **2018**, *8*, 57. [[CrossRef](#)]
11. Upadhyay, L.S.B.; Verma, N. Enzyme inhibition based biosensors: A review. *Anal. Lett.* **2013**, *46*, 225–241. [[CrossRef](#)]
12. Trojanowicz, M.; Hitchman, M.L. Determination of pesticides using electrochemical biosensors. *TrAC Trends Anal. Chem.* **1996**, *15*, 38–45. [[CrossRef](#)]
13. Barceló, D.; Hennion, M. Sampling of polar pesticides from water matrices. *Anal. Chim. Acta* **1997**, *338*, 3–18. [[CrossRef](#)]
14. Kumaran, S.; Morita, M. Application of a cholinesterase biosensor to screen for organophosphorus pesticides extracted from soil. *Talanta* **1995**, *42*, 649–655. [[CrossRef](#)]
15. Gahlaut, A. Electrochemical biosensors for determination of organophosphorus compounds. *Open J. Appl. Biosens.* **2012**, *1*, 1. [[CrossRef](#)]
16. Pundir, C.; Malik, A. Preety Bio-sensing of organophosphorus pesticides: A review. *Biosens. Bioelectron.* **2019**, *140*, 111348. [[CrossRef](#)]
17. Dhull, V.; Gahlaut, A.; Dilbaghi, N.; Hooda, V. Acetylcholinesterase biosensors for electrochemical detection of organophosphorus compounds: A review. *Biochem. Res. Int.* **2013**, *2013*, 731501. [[CrossRef](#)]
18. Yongliang, Z.; Lifang, L.; Yuanyuan, F.; Jianping, G.; Jianping, F.; Weibin, J.; Zheng, Y.; Long, L.; Fan, Y.; Gan, J.; et al. A review on the detoxification of organophosphorus compounds by microorganisms. *Afr. J. Microbiol. Res.* **2013**, *7*, 2127–2134. [[CrossRef](#)]
19. Pohanka, M. Acetylcholinesterase inhibitors: A patent review (2008–present). *Expert Opin. Ther. Patents* **2012**, *22*, 871–886. [[CrossRef](#)]
20. Pundir, C.S.; Chauhan, N. Acetylcholinesterase inhibition-based biosensors for pesticide determination: A review. *Anal. Biochem.* **2012**, *429*, 19–31. [[CrossRef](#)]
21. Robb, E.L.; Baker, M.B. Organophosphate toxicity. *Nurse Pract.* **2017**, *46*, 18–21. [[CrossRef](#)]
22. Xu, M.-L.; Gao, Y.; Han, X.X.; Zhao, B. Detection of pesticide residues in food using surface-enhanced Raman spectroscopy: A review. *J. Agric. Food Chem.* **2017**, *65*, 6719–6726. [[CrossRef](#)]
23. Palchetti, I.; Laschi, S.; Mascini, M. Electrochemical biosensor technology: Application to pesticide detection. In *Biosensors and Biodetection*; Springer: Berlin/Heidelberg, Germany, 2009; pp. 115–126.
24. Zhang, S.; Zhao, H.; John, R. A theoretical model for immobilized enzyme inhibition biosensors. *Electroanal. Int. J. Devoted Fundam. Pract. Asp. Electroanal.* **2001**, *13*, 1528–1534. [[CrossRef](#)]
25. Choi, J.-W.; Min, J.; Lee, W.-H. Signal analysis of fiber-optic biosensor for the detection of organophosphorus compounds in the contaminated water. *Korean J. Chem. Eng.* **1997**, *14*, 101–108. [[CrossRef](#)]
26. Rafat, N.; Satoh, P.; Barton, S.C.; Worden, R. Integrated Experimental and Theoretical Studies on an Electrochemical Immunosensor. *Biosensors* **2020**, *10*, 144. [[CrossRef](#)]
27. Kohli, N.; Srivastava, D.; Sun, J.; Richardson, R.J.; Lee, I.; Worden, R.M. Nanostructured Biosensor for measuring neuropathy target esterase activity. *Anal. Chem.* **2007**, *79*, 5196–5203. [[CrossRef](#)] [[PubMed](#)]
28. Richardson, R.J.; Fink, J.K.; Worden, R.M.; Wijeyesakere, S.J.; Makhaeva, G.F. Neuropathy target esterase as a biomarker and biosensor of delayed neuropathic agents. In *Handbook of Toxicology of Chemical Warfare Agents*; Elsevier: Amsterdam, The Netherlands, 2020; pp. 1005–1025.
29. Kohli, N.; Lee, I.; Richardson, R.J.; Worden, R.M. Theoretical and experimental study of bi-enzyme electrodes with substrate recycling. *J. Electroanal. Chem.* **2010**, *641*, 104–110. [[CrossRef](#)]
30. Ruan, C.; Li, Y. Detection of zeptomolar concentrations of alkaline phosphatase based on a tyrosinase and horse-radish peroxidase bienzyme biosensor. *Talanta* **2001**, *54*, 1095–1103. [[CrossRef](#)]

31. Kulys, J.; Baronas, R. Modelling of amperometric biosensors in the case of substrate inhibition. *Sensors* **2006**, *6*, 1513–1522. [[CrossRef](#)]
32. Baronas, R.; Kulys, J.; Lančinskas, A.; Žilinskas, A. Effect of diffusion limitations on multianalyte determination from biased biosensor response. *Sensors* **2014**, *14*, 4634–4656. [[CrossRef](#)]
33. Baronas, D.; Ivanauskas, F.; Baronas, R. Mechanisms controlling the sensitivity of amperometric biosensors in flow injection analysis systems. *J. Math. Chem.* **2011**, *49*, 1521–1534. [[CrossRef](#)]
34. Irie, T.; Fukushi, K.; Iyo, M. Evaluation of phenylmethanesulfonyl fluoride (PMSF) as a tracer candidate mapping acetylcholinesterase in vivo. *Nucl. Med. Biol.* **1993**, *20*, 991–992. [[CrossRef](#)]
35. Kraut, D.; Goff, H.; Pai, R.K.; Hosea, N.A.; Silman, I.; Sussman, J.; Taylor, P.; Voet, J.G. Inactivation studies of acetylcholinesterase with phenylmethylsulfonyl fluoride. *Mol. Pharmacol.* **2000**, *57*, 1243–1248.
36. Coche-Guerente, L.; Labbé, P.; Mengers, V. Amplification of Amperometric Biosensor Responses by Electrochemical Substrate Recycling. 3. Theoretical and Experimental Study of the Phenol–Polyphenol Oxidase System Immobilized in Laponite Hydrogels and Layer-by-Layer Self-Assembled Structures. *Anal. Chem.* **2001**, *73*, 3206–3218. [[CrossRef](#)] [[PubMed](#)]
37. Parthasarathy, P.; Vivekanandan, S. A numerical modelling of an amperometric-enzymatic based uric acid biosensor for GOUT arthritis diseases. *Inform. Med. Unlocked* **2019**, *16*, 100233. [[CrossRef](#)]
38. Ismail, I.; Oluleye, G.; Oluwafemi, I. Mathematical modelling of an enzyme-based biosensor. *Int. J. Biosens. Bioelectron.* **2017**, *3*, 265–268.
39. Kacser, H.; Burns, J.A.; Fell, D.A. *The Control of Flux*; Portland Press Limited: London, UK, 1995.